

Simulation and experimentation of a microfluidic device based on electrowetting on dielectric

Ling-Sheng Jang · Guo-Hua Lin · Yi-Liang Lin ·
Chih-Yuan Hsu · Wai-Hong Kan · Chiun-Hsun Chen

Published online: 23 May 2007
© Springer Science + Business Media, LLC 2007

Abstract Electrowetting on dielectric (EWOD) moving fluid by surface tension effects offers some advantages, including simplicity of fabrication, control of minute volumes, rapid mixing, low cost and others. This work presents a numerical model using a commercial software, CFD-ACE+, and an EWOD system including a microfluidic device, a microprocessor, electric circuits, a LCD module, a keypad, a power supply and a power amplifier. The EWOD model based on a reduced form of the mass conservation and momentum equations is adopted to simulate the fluid dynamics of the droplets. The EWOD device consists of the 2×2 mm bottom electrodes (Au/Cr), a dielectric layer of 3,000 Å nitride, 500 Å Teflon and a piece of indium tin oxide (ITO)-coated glass as the top electrode. The complete EWOD phenomenon is elucidated by comparing simulation with the experimental data on droplet transportation, cutting and creation. In transportation testing, the speed of the droplet is 6 mm/s at 40 V_{dc}. In addition, the droplet division process takes 0.12 s at 60 V_{dc} in the current case. Finally, a 347 nl droplet is successfully created from an on-chip reservoir at 60 V_{dc}.

Keywords Microfluidics · Electrowetting · EWOD · Surface tension

1 Introduction

Microfluidics refers to miniaturized analysis systems for chemical and biological applications. The growing importance of proteomics, genomics and drug discovery implies that microfluidic systems have become an important focus for research. Microfluidic systems, such as lab-on-a-chip, adopt MEMS (Microelectromechanical system) technology for the small size, high throughput, rapid response, low cost, low power consumption, reduction in reagents and small dead volume. Many microfluidic devices have been developed to manipulate fluids on the microscale (Reyes et al. 2002; Auroux et al. 2002). In these devices, the approaches to control the movement of fluids can be classified as being either mechanical or non-mechanical micropumping. Most of the mechanical micropumps are composed of reciprocating membranes and valves. Many methods have been introduced to operate, i.e., pressurize mechanical micropumps, including pneumatic (Liao et al. 2005), thermopneumatic (Tsai and Lin 2002), electrostatic (Xie et al. 2004), piezoelectric (Jang et al. 2007), electromagnetic (Ahn and Allen 1995), shape memory alloy (Shu 2002), and so on. The non-mechanical pumps add momentum to the fluid for pumping effect by converting another energy form into the kinetic energy. Several fluidic driving mechanisms without mechanical pumps and valves have been demonstrated, such as acoustic-wave pumps (Yu and Kim 2002), electroosmotic pumps (Selvaganapathy et al. 2002), electrohydrodynamic (EHD) pumps (Bart et al. 1990), bubble or droplet pumps utilizing thermocapillary (Sammarco and Burns 1999), and electrowetting-based pumps (Kim 2001).

L.-S. Jang (✉) · C.-Y. Hsu · W.-H. Kan
Department of Electrical Engineering and Center for Micro/Nano
Science and Technology, National Cheng Kung University,
1 University Road, Tainan 701, Taiwan
e-mail: lsjang@ee.ncku.edu.tw

G.-H. Lin · C.-H. Chen
Department of Mechanical Engineering, National Chiao Tung
University, Hsinchu, Taiwan

L.-S. Jang · Y.-L. Lin
Institute of Nanotechnology and Microsystems Engineering,
National Cheng Kung University, Tainan, Taiwan

It has been known for over a century that heat (thermocapillary) and electrical potential (electrocapillary) (Lippman 1875) can be used to change the surface tension, and flow can be induced as a result. As MEMS technologies advanced in recent years, much attention has been drawn to using surface tension, which becomes a dominant force on the microscale, for the microfluidic actuation (Cho et al. 2003). Micropumping has been reported using thermal control of surface tension, i.e., thermocapillary. Compared to thermocapillary, however, electrocapillary, involving no heating of the liquid, is much more energy efficient and advantageous for most microfluid actuations. In different device configurations, electro-capillary may be referred to as continuous electrowetting (CEW), electrowetting (EW), or electrowetting on dielectric (EWOD) (Zeng and Korsmeyer 2004). CEW needs a liquid metal (e.g. mercury) in a filler liquid (certain electrolytes), and creates a non-uniform interfacial tension at the two-fluid interface. The induced interfacial shear flow can be used to move the droplets. Examples are reflective displays (Roques-Carnes et al. 2004), optical switch (Beni et al. 1982), tunable optical fiber devices (Cattaneo et al. 2003) and rotating liquid micromotor (Lee and Kim 2000). Since CEW requires two liquids, the process becomes complex, potentially damaging the samples. EW drives flow in a channel by varying the surface tension, which depends on the electrical double layer (EDL) between the interface of the channel, air and the liquid. Since the droplet is in contact with a solid electrode, electrolysis may occur when a large voltage is applied. Therefore, the strength of the wetting force is limited. However, an insulating layer can be coated on the electrode to increase the voltage at which electrolysis occurs, thus allowing a higher wetting force. The electric field controls the wettability of liquids on a dielectric material, in a process called electrowetting on dielectric (EWOD) which has become one of the most promising configurations for digital microfluidics.

Droplet-based microfluidic systems using EWOD differ from continuous flow systems because they manipulate discrete droplets rather than a continuous flow. EWOD exhibits excellent reversibility and has many advantages over continuous-flow systems, including the capacity to control each droplet independently, minimize the usage of fluids and reduce the mixing time. Applications of these devices include micro-fluid transporting (Cho et al. 2003), mixing, dispensing (Ren et al. 2004), and sensing of biological samples (Srinivasan et al. 2003). It has been shown that the droplets in the order of tens of nanoliters can be displaced on the chip surface in a controllable manner so that the basic manipulations of EWOD for biological treatments can be performed. The key manipulations of the droplet are transportation from one electrode to the next one, cutting into two “daughter” drops and creation from

the reservoir on the chip. Additionally, the volume of the micro-drops may be carefully controlled. In order to facilitate the development of such microsystems, it is necessary to develop a numerical model which involves the physical phenomena in electrowetting. To do so, a simulation-based investigation of the basic manipulations in an EWOD systems was initiated. The simulation study was directly structured to perform the transportation, cutting and creation of the droplet from the reservoir.

In this study, a numerical model using a commercial software “CFD-ACE+” was first proposed. Additionally, an EWOD system based on a microprocessor was successfully developed. The system was used to perform fundamental functions such as transportation, cutting and creation of the droplet. Finally, this work presents the comparison of results simulated using CFD-ACE+ and made using the EWOD system.

2 The principle of electrowetting

It has been observed that a droplet spreads until it has reached a minimum free energy, determined by cohesive forces in the liquid and adhesion between the liquid and the surface. The energy required to form an interface is determined by the surface tension (N/m) or surface free energy (J/m²) (γ). According to the work published by Verheijen and Prins (1999), when a potential is applied, change in the electric charge distribution at the liquid/solid interface alters the free energy on the dielectric surface, inducing a change in wettability on the surface and contact angle of the droplet (Fig. 1(a)). Figure 1(b) presents the edge of a droplet and its virtual displacement. An infinitesimal increase of the base area dA results in a contribution to the free energy from the surface energies. The free energy (F) of the system can be written in differential form:

$$dF = \gamma_{SL}dA - \gamma_{SG}dA + \gamma_{LG}dA \cos \theta + dU_e \quad (1)$$

where U_e represents the energy required to establish an electric field between the liquid and the counter electrode. γ is interfacial tension of interface, in which the subscript L, G and S denotes liquid, gas and solid phases, respectively. The contact angle θ is that between the liquid/gas interface and the solid/liquid interface at the contact line. In the first situation, no external voltage is applied. Equilibrium and an energy minimum are reached when $U_e=0$ and $dF/dA=0$, yielding Young’s equation,

$$\gamma_{SL} = \gamma_{SG} - \gamma_{LG} \cos \theta \quad (2)$$

$$\cos \theta = \frac{\gamma_{SG} - \gamma_{SL}}{\gamma_{LG}} \quad (3)$$

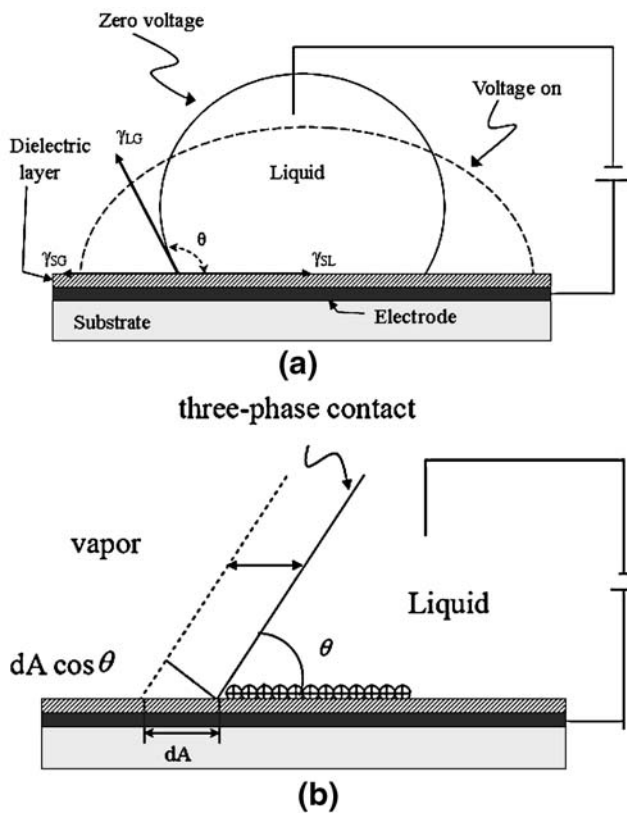


Fig. 1 Principle of electrowetting on dielectric (EWOD). **(a)** Schematic configuration. **(b)** Virtual displacement of the contact line in the presence of a potential across the dielectric layer

Since the electrical double layer (EDL) is like the parallel plate capacitor, when an external voltage is applied, the EDL stores energy. This stored energy may be written as

$$U = \frac{Q^2}{2C} \tag{4}$$

where Q is the magnitude of the charge on either conductor and C is the capacitance of the parallel-plate capacitor. $C = Q/V$ is used in Eq. 4 to determine the stored energy in terms of voltage:

$$U = \frac{Q^2}{2C} = \frac{(CV)^2}{2C} = \frac{1}{2} CV^2 \tag{5}$$

Since only a small voltage drop can be sustained across the EDL, the change in the contact angle ($\Delta\theta$) that can be induced by conventional electrowetting is relatively small. A thin dielectric layer inserted between the electrode and the liquid was discovered recently to emulate the EDL in conventional electrowetting. This principle is called electrowetting on dielectric. Many articles have discussed the relationship between the external voltage and the surface

tension of EWOD. These results are expressed by Lippmann’s equation (Lippman 1875);

$$\gamma = \gamma_0 - \frac{1}{2} cV^2 \tag{6}$$

Lippman’s equation specifies the relationship between the surface tension and the electric potential, where d is dielectric of thickness, γ_0 is the surface tension of the solid–liquid interface at zero charge and c is the capacitance per unit area ($c = C/A$). Lippmann’s equation (6) can be expressed in terms of the contact angle θ by incorporating Young’s equation (2). The resulting equation (7) is called the Lippman–Young’s equation:

$$\begin{aligned} \cos \theta_V - \cos \theta_0 &= \frac{\gamma_{SG} - \gamma_{SL} + \frac{1}{2}cV^2}{\gamma_{LG}} - \frac{\gamma_{SG} - \gamma_{SL}}{\gamma_{LG}} \\ &= \frac{1}{2} \frac{1}{\gamma_{LG}} cV^2 \\ \cos \theta_V - \cos \theta_0 &= \frac{1}{2} \frac{\epsilon_0 \epsilon_r}{d\gamma_{LG}} V^2 \end{aligned} \tag{7}$$

3 Numerical approach

A commercial code, CFD-ACE+ (CFD Research Corporation), was used to create a model based on the principle of EWOD. The code offers unique capabilities for multiphysics, multiscale, and coupled simulations of fluid, thermal, chemical, biological, electrical, and mechanical phenomena for real-world applications. The geometric model of the EWOD device was constructed using GEOM of CFD-ACE+ software. The boundary conditions and analysis model were defined using the ACE(U) module in the program. In these simulations, the volume-of-fluid (VOF) technique was applied to simulate the liquid–gas interface. Figure 2 displays the top view of an EWOD model; a circular droplet is observed when no voltage is applied.

3.1 Flow module

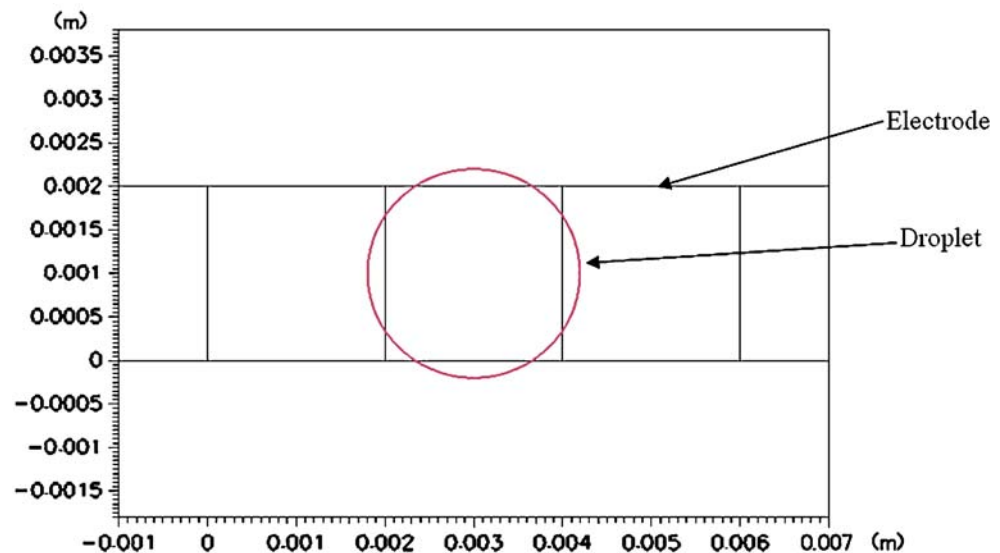
The governing equations of the Flow Module are mathematical statements of the conservation laws for flow.

- The mass of a fluid is conserved.
- The rate of change of momentum equals the sum of the forces on the fluid (Newton’s second law).

These two laws are adopted to develop a set of equations (known as the Navier–Stokes equations) for CFD-ACE+ to be solved numerically. Conservation of mass requires that the time rate of change of mass in a control volume be balanced by the net mass flow into the same control volume:

$$\frac{\partial \rho}{\partial t} + \nabla \cdot (\rho \vec{V}) = 0 \tag{8}$$

Fig. 2 Top view of an EWOD model



The fundamental equations of momentum conservation are as follows:

$$\begin{aligned} \frac{\partial u}{\partial t}(\rho u) + \nabla \cdot \rho \vec{V} u &= -\frac{\partial p}{\partial x} + \frac{\partial}{\partial x} \left[2\mu \frac{\partial u}{\partial x} \right] \\ &+ \frac{\partial}{\partial y} \left[\mu \left(\frac{\partial v}{\partial x} + \frac{\partial u}{\partial y} \right) \right] \\ &+ \frac{\partial}{\partial z} \left[\mu \left(\frac{\partial u}{\partial z} + \frac{\partial w}{\partial x} \right) \right] + F_x^\sigma + \rho a_x \end{aligned} \quad (9)$$

$$\begin{aligned} \frac{\partial u}{\partial t}(\rho v) + \nabla \cdot \rho \vec{V} v &= -\frac{\partial p}{\partial y} + \frac{\partial}{\partial x} \left[\mu \left(\frac{\partial v}{\partial x} + \frac{\partial u}{\partial y} \right) \right] \\ &+ \frac{\partial}{\partial y} \left[2\mu \frac{\partial v}{\partial y} \right] \\ &+ \frac{\partial}{\partial z} \left[\mu \left(\frac{\partial v}{\partial z} + \frac{\partial w}{\partial y} \right) \right] + F_y^\sigma + \rho a_y \end{aligned} \quad (10)$$

$$\begin{aligned} \frac{\partial w}{\partial t}(\rho w) + \nabla \cdot \rho \vec{V} w &= -\frac{\partial p}{\partial z} + \frac{\partial}{\partial x} \left[\mu \left(\frac{\partial u}{\partial z} + \frac{\partial w}{\partial x} \right) \right] \\ &+ \frac{\partial}{\partial z} \left[\mu \left(\frac{\partial v}{\partial z} + \frac{\partial w}{\partial y} \right) \right] \\ &+ \frac{\partial}{\partial z} \left[2\mu \left(\frac{\partial w}{\partial z} \right) \right] + F_z^\sigma + \rho a_z \end{aligned} \quad (11)$$

where ρ (kg/m^3) denotes density, μ (N s/m^2) is viscosity, P (Pa) is the pressure of the water droplet relative to air, V (m/s) is velocity, F_z^σ is the surface tension (N/m), and ρa_z (m/s^2) is the acceleration due to gravity.

3.2 Free surface module

The basis of the approach employed by the free surface module is volume-of-fluid (VOF), published in an early form elsewhere (Hirt and Nichols 1981) and recently extended (Rider et al. 1995). The model can accommodate any two fluids that are incompressible and immiscible and between which localized slip is negligible. Water and air (when compressibility is insignificant) are good examples. In this study, a VOF interface tracking method proposed by Hirt and Nichols is adopted to represent the fluid domain and track the evolution of the domain's free boundaries.

The defining characteristic of the VOF methodology is that the distribution of the second fluid (such as water) in the computational grid is described by a single scalar field variable, F , which specifies the fraction of the volume of each computational cell in the grid that is occupied by the second fluid (water). Thus, F takes the value one in cells that contain only fluid 2 (water) and the value zero in cells that contain only fluid 1 (air). A cell that contains an interface would have an F value of between zero and one. The manner in which the volume fraction distribution F (and hence the distribution of fluid 2) evolves is determined by solving the passive transport equation.

$$\frac{\partial F}{\partial t} + \nabla \cdot \vec{v} F = 0 \quad (12)$$

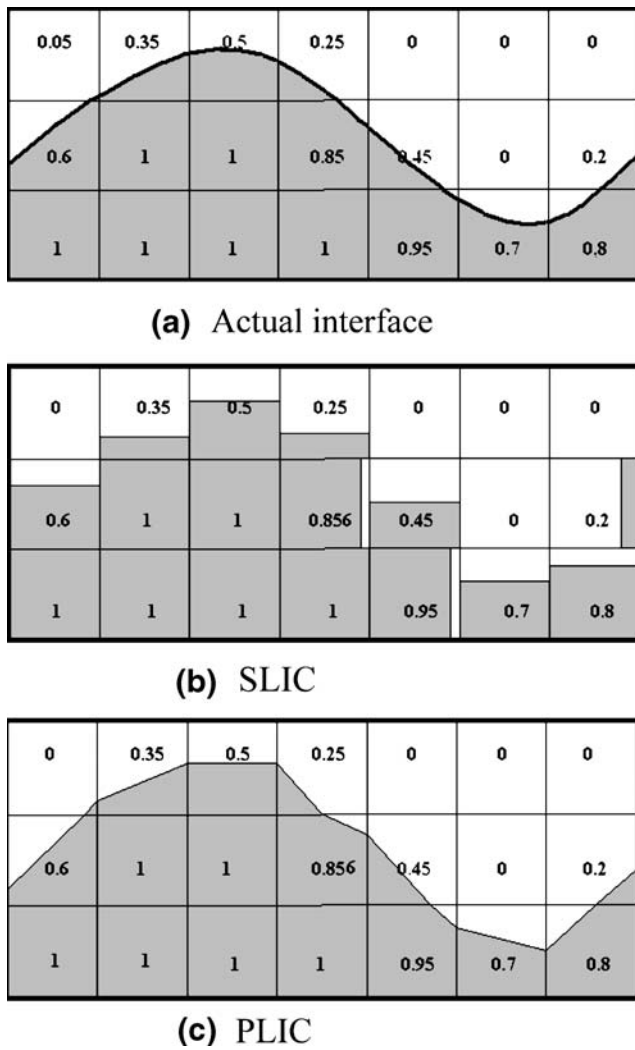


Fig. 3 Schematic diagram of free surface reconstructions: (a) actual interface; (b) SLIC approximation; (c) PLIC approximation

where F is the liquid volume fraction, t is time, ∇ is the standard spatial grad operator, and \vec{v} is the velocity vector. This equation must be solved together with the fundamental equations of conservation of mass and momentum in CFD-ACE+ to achieve computational coupling between the velocity field solution and the liquid distribution.

In the CFD-ACE+ code, surface reconstruction is a prerequisite for determining the flux of fluid two from one cell to the next, and for determining surface curvatures when the surface tension model is activated. The following two approaches to surface reconstruction are currently available.

- Single Line Interface Construction (SLIC) Method (Noh and Woodward 1976)
- Piecewise Linear Interface Construction (PLIC) Method (Youngs 1982)

The original SLIC method approximates the interface in each mesh cell as a line that is parallel to one of the

coordinate axes in a two-dimensional analysis, as shown in Fig. 3(b). However, the representation of the interface using SLIC is rough. The piecewise-linear interface calculation (PLIC) technique proposed by Youngs represents a useful refinement to the SLIC method, using a straight line to approximate the interface in each computational cell, as displayed in Fig. 3(c). The PLIC method is adopted and then coupled to the VOF method in this work (Rider and Kothe 1998; Gueyffier et al. 1999; Scardovelli and Zaleski 2000).

3.3 SIMPLEC algorithm

Solutions to the three momentum equations yield the three Cartesian components of velocity. Pressure-based approaches use the continuity equation to formulate an equation for pressure. In the CFD-ACE+ code, the SIMPLEC scheme is adopted. SIMPLEC stands for Semi-Implicit Method for Pressure-Linked Equations Consistent, and represents an

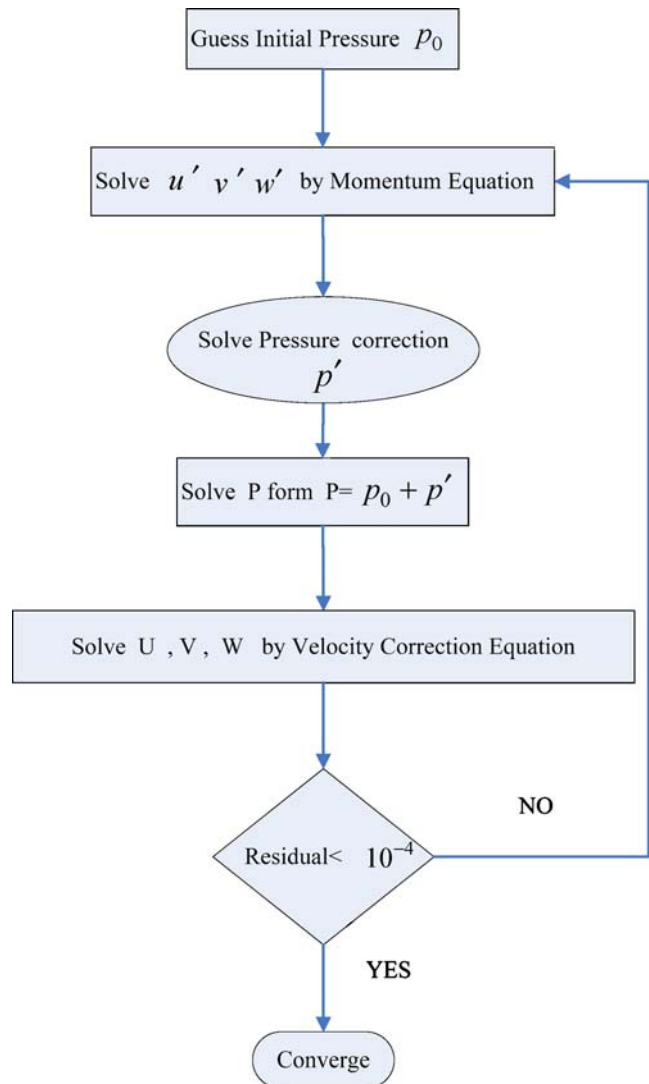


Fig. 4 SIMPLEC algorithm

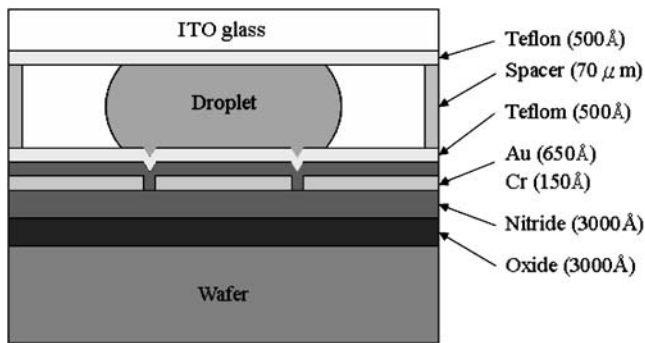


Fig. 5 Schematic of cross-sectional view of the device

enhancement of the well known SIMPLEC algorithm. In SIMPLEC originally proposed by Van Doormaal and Raithby in 1984, an equation for pressure-correction is derived from the continuity equation. It is an inherently iterative method. Figure 4 summarizes the SIMPLEC procedure.

4 Fabrication

Figure 5 shows the cross-sectional view of the device. Each device was formed from a bottom plate with individually addressable electrodes and a top plate fabricated as a single, large electrode. The process began with a 4", N type, 500 μm thick (100) silicon wafer. The wafer was covered by a layer of 3,000 Å oxide (SiO₂) and 3,000 Å silicon nitride (Si₃N₄) as insulator using plasma-enhanced chemical vapor deposition (PECVD). A layer of 150 Å chromium and 650 Å gold were evaporated by E-beam evaporator and patterned by photolithography as the bottom electrodes with the dimensions of 2×2 mm. The electrodes were covered by a dielectric layer of silicon nitride (3,000 Å) using PECVD. Thin dielectric layers enable droplet actuation at low applied voltage and avoid electrolysis and bubble formation. The silicon nitride on the electrode contact pads of the devices was etched by H₃PO₄. The devices were then spin-coated with hexamethyldisilazane (HMDS, 4,000 rpm, 50 s) and 1% Teflon-AF (3,000 rpm, 30 s). The devices were post-baked on a hotplate (160°C, 10 min) and in a furnace (260°C, 30 min) to produce a uniform ~500 Å layer of Teflon-AF. The top plate was formed from indium tin oxide (ITO)-coated glass. A 500 Å-thick layer of Teflon-AF was spin-coated on the ITO coated glass. The two plates were joined using 3M double-sided tape as a spacer to produce a gap with the height of 70 μm. A 0.5 μl droplet of deionized water was sandwiched between the two plates and actuated by the applied voltage between the electrode on the top plate and successive electrodes on the bottom plate. Droplet motion was observed using a microscope (Eclipse 50i, Nikon) and recorded by a color video camera (SSC-DC80, Sony).

5 Contact angle measurement

Measurements of the contact angle change by EWOD were made in a water droplet using Contact Angle Goniometer (MagicDrop, USA). The droplet was placed on a 3,000 Å dielectric layer of silicon nitride coated with 500 Å Teflon. A wire was penetrated into the droplet from the top, and the dc potential was applied between the liquid and the electrode underneath the dielectric layers. The dielectric layers of nitride and Teflon formed two plate capacitors in series. The capacitance of a single capacitor is given by,

$$c = \frac{\epsilon_r \epsilon_0}{d} \quad (13)$$

where c is the capacitance per unit area. The equivalent capacitance of two capacitors in series can be obtained from the following.

$$\frac{1}{c} = \frac{1}{c_1} + \frac{1}{c_2} \quad (14)$$

The dielectric constant (ϵ_r) of 3,000 Å nitride and 500 Å Teflon is 7.8 and 2, respectively. The equivalent capacitance of the nitride and Teflon layers can be obtained by Eqs. 13 and 14. Figure 6 shows the comparison of the experimental and theoretical contact angles based on Eq. 7. The contact angle parabolically decreases as the applied potential increases until is saturated between 70° and 80°. The reason for the saturation is not clearly understood as of today. In any case, there exists a limitation in the contact angle change by EWOD, beyond which higher potential does not decrease the contact angle any further. In addition, the Lippmann–Young's equation does not consider the proceeding of the droplet. However, the droplet is advancing with the applied voltage. Accordingly, the energy is dissipated in the spreading process, leading to a lower predicted contact angle.

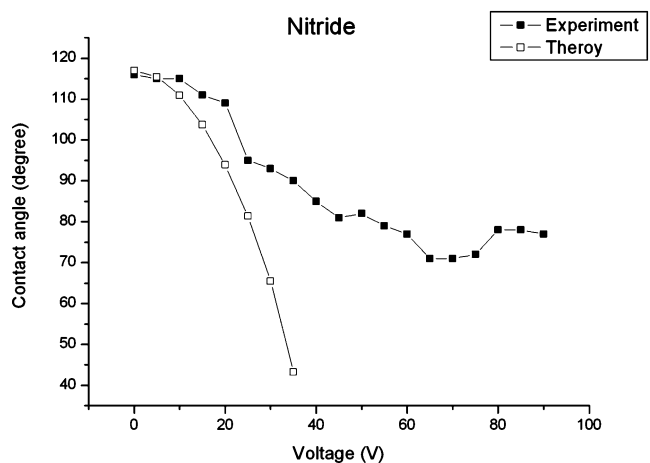


Fig. 6 Measurements of the contact angle change by EWOD in a water droplet on a 3,000 Å dielectric layer of silicon nitride coated with 500 Å Teflon

6 Driving system

Figure 7 presents the block diagram of the driving system. The driving system consisted of a microcontroller (AVR® ATmega8535), electric circuits (eight BJTs), a LCD module (SC1602A), a keypad, a power supply (MOTTECH LPS-305) and a power amplifier (AVL instrumentation Inc. 790 series). The driving signal generated by a power supply was amplified using a power amplifier and then was delivered to BJTs (MPSA44). The microprocessor was programmed to generate signal voltages which switched the transistors between cut-off and saturation. Applying a voltage to the base of BJT enabled BJT to operate as a switch. Thus, BJTs were employed to generate the sequences of driving voltages for the EWOD chip. The microprocessor with high-performance and low-power AVR® 8-bit microcontroller manufactured by ATMEL was the main component of the driving circuits. The microprocessor had several functions, including a self-programming memory, multiple instructions and a debug interface. The code was written in the C language, and embedded in the microprocessor. The LCD module received character codes from the microprocessor, and latched them to its display data RAM. Each character code was then transformed into a character, which was displayed on the screen.

7 Results and discussion

The meshing elements and accuracy of the numerical model (Fig. 2) was determined by the testing of grid density. The convergence criteria of simulation is 0.0001 (four orders of magnitude) which is the minimum reduction in residuals for each variable. Figure 8 presents the grid density of the numerical model versus the pressure difference in the liquid between the left and right interfaces, which is the pumping pressure for the motion of the liquid droplet. According to Fig. 8, the

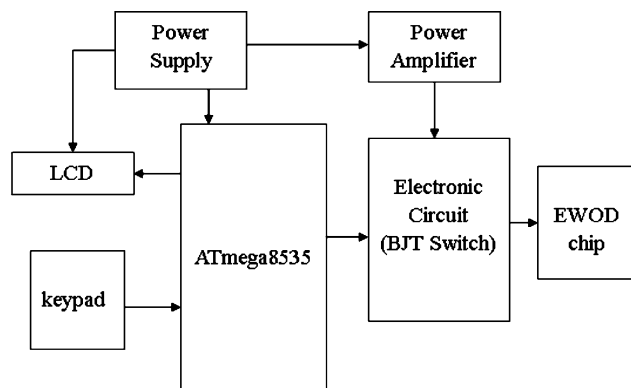


Fig. 7 Block diagram of the driving system

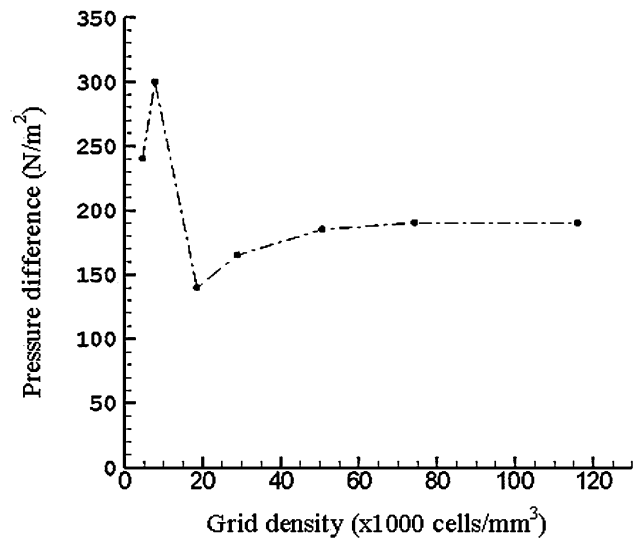


Fig. 8 Evolution of the pressure difference against grid density

pressure difference reached a stable value, 190 N/m², at a grid density of 74,286 cells/mm³, which was used in the simulations. The numerical pressure difference was compared with the theoretical result. The pressure difference (612 N/m²) was theoretically calculated based on Eq. 15, where P_L is the pressure of the liquid at the left interface, P_R is the pressure of the liquid at the right interface, γ_{LG} is the surface tension at the interface of the liquid and air (0.0719 N/m), h is the channel height (70 μ m), θ_v is the contact angle at a voltage (80° at 40 V) and θ_0 is the contact angle at zero voltage (115° at 0 V). Equation 15 is derived based on Fig. 9 by Lee et al. (2002). The variation between the simulation and theoretical results may come from the assumptions of the theoretical model. The theoretical model does not consider the dynamic effects of contact angle change and assumes that the droplet is in a static equilibrium during the derivation. Additionally, the theoretical model is two dimensional and does not consider the viscous force. Therefore, it results in a higher pressure difference than the numerical model.

$$\Delta P = P_L - P_R = \frac{\gamma_{LG}}{h} (\cos \theta_v - \cos \theta_0) \tag{15}$$

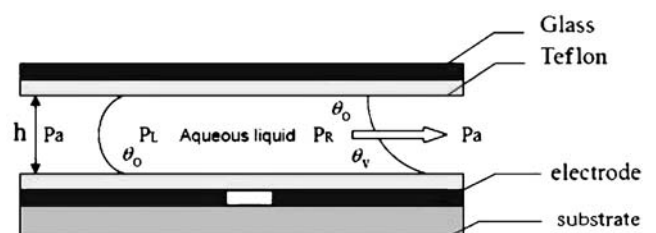


Fig. 9 Contact angles of the droplet driven by EWOD

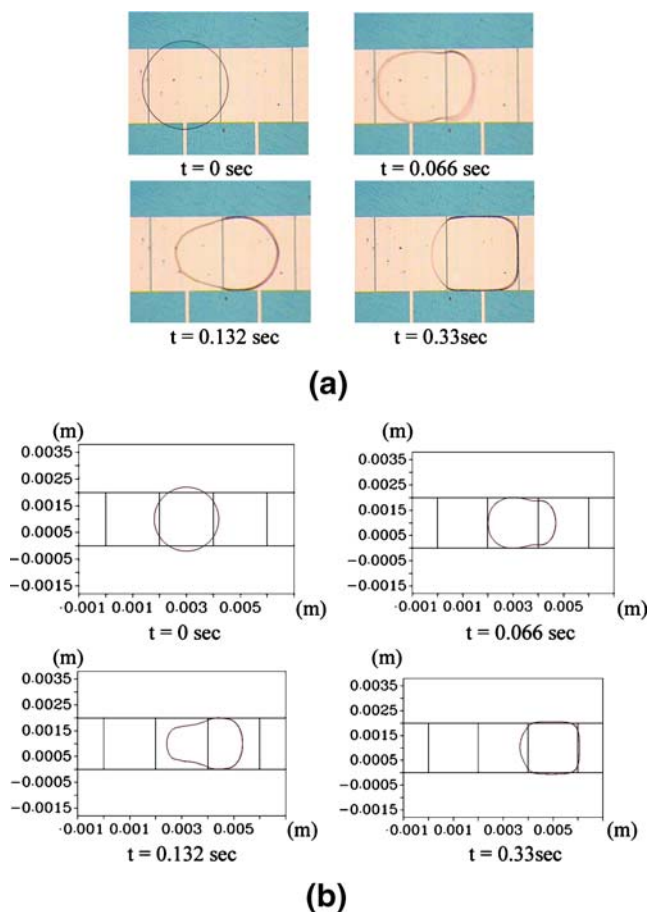


Fig. 10 Transportation of a droplet at 40 V_{dc} : (a) experimental results; (b) simulation results

A discrete droplet in a channel can be moved by asymmetrically changing the interfacial tension. The asymmetric change in the interfacial tension induces an asymmetric deformation of the liquid meniscus, which establishes a pressure difference inside liquid, giving a rise to bulk fluid movement. The experiment demonstrates that the movement of droplet was initiated at 40 V_{dc} . Transportation was verified by sequentially energizing the electrode beneath the leading meniscus of the droplet. Figure 10 shows the experimental and numerical results of droplet transportation. The droplet remained circular when no voltage was applied. When the right electrode was activated, the droplet began to move to the next electrode due to the pressure difference associated with EWOD. The transporting speed was about 6 mm/s at 40 V_{dc} .

Figure 11 shows the numeric and experimental results of droplet cutting. Droplet division was successfully performed at 60 V_{dc} . It was initiated by the elongation of the droplet in the longitudinal direction and necking in the middle of the droplet. In the beginning, the droplet occupied the entire middle electrode as well as a portion of each control electrode at the ends. During stretching,

the left and right electrodes were energized to make the two ends wetting so the contact angles reduced according to Eq. 7. In the mean time, the middle electrode was grounded, keeping the middle section nonwetting (hydrophobic). Consequently, the meniscus on the middle electrode started to contract in order to keep the total volume of the droplet constant. Finally, the neck was pinched off and cutting occurred. In this case, the total cutting process took 0.12 s.

To create a droplet from a reservoir on chip, liquid has to be first pulled out of the reservoir and separated from it. Figure 12(a) demonstrates that the droplet could be created from a reservoir droplet by pulling liquid out along the electrode path at an applied voltage of 60 V_{dc} . The process of droplet creation was highly associated with the cutting process. When the front meniscus of liquid was pulled out of the reservoir by EWOD, the liquid continued to follow the leading meniscus to form a liquid column. Three control electrodes were used to complete the droplet creation as shown in Fig. 12(a). The switching interval of the electrodes was 1 s. The first and second electrodes were sequentially activated from the right to the left. When the front end of the column reached the third electrode, the first and third electrodes were activated and the second electrode was turned off. The electrode in the reservoir was also activated to generate a sufficient pressure difference to complete the cutting. Accordingly, droplet necking occurred on the second electrode and then the liquid column

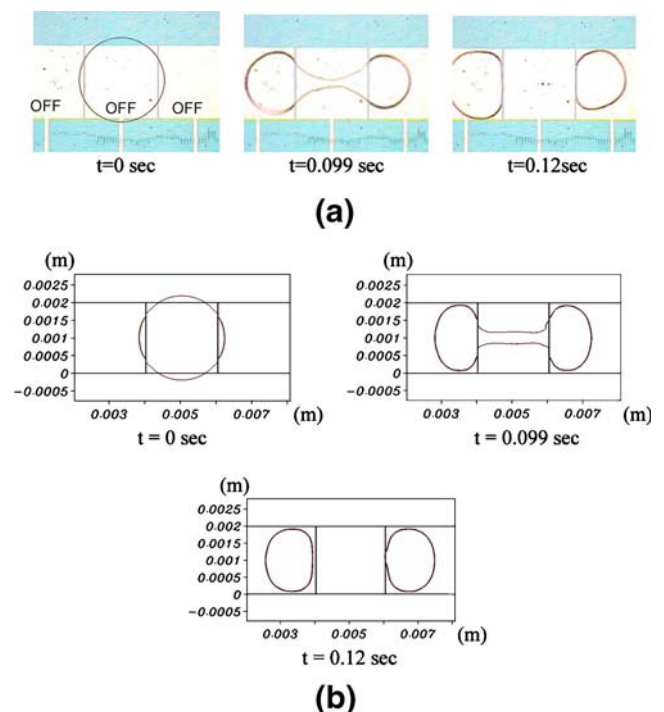


Fig. 11 Cutting of a droplet at 60 V_{dc} : (a) experimental results; (b) simulation results

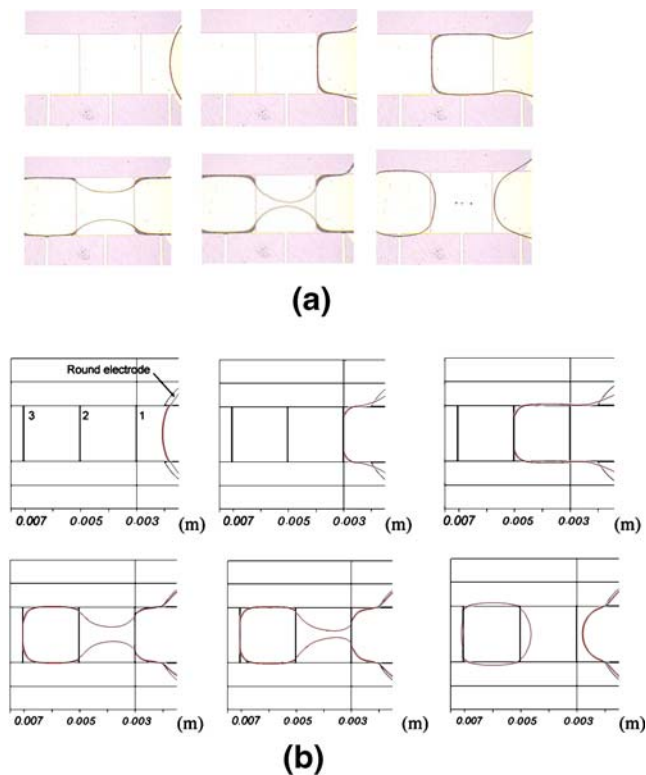


Fig. 12 Droplet creation from a reservoir at 60 V_{dc}: (a) experimental results; (b) simulation results

was pulled back to the reservoir. The captured image of the created droplet was used to determine the cross-sectional area of the droplet by AutoCAD. The volume of the droplet was around 347 nl obtained by the product of the cross-sectional area and the channel height. Figure 12(b) indicates that the numerical model successfully simulated the process of droplet creation.

According to Figs. 10, 11 and 12, there are some differences between the experimental and computational results. The variations may result from several factors during the experimental process. For instance, the water droplet is difficult to be precisely placed in the center of the electrode. The location of the droplet on the electrodes is different for each test. Additionally, the volume of the water droplet varies from case to case. The droplet starts to vaporize after the droplet is generated and placed on the bottom plate by a pipette. Thus the volume of the droplet is not the exactly same as desired for each test. Moreover, the channel gap is created by the double-sided tape with a height of 70 μm. If two plates are placed too hard by fingers, the height of the channel will be lower than 70 μm. The other factor is the roughness of the surface. The dielectric layer (Teflon) is spin-coated and baked in a furnace. The fabrication process may result in rough surface and introduce the fiber dust to the Teflon surface. These

experimental errors may lead to deviation between the experimental and computational results.

8 Conclusions

A numerical model of EWOD was first developed by CFD-ACE+. Transportation, division and creation of a droplet were successfully simulated based on the model. Additionally, an EWOD system consisting of a microfluidic device, a microprocessor, electric circuits, a LCD module, a keypad, a power supply and a power amplifier was developed. Measurements of the contact angle change by EWOD were made to find the saturation region. Moreover, transportation, division and creation of a droplet were experimentally performed using this system. The simulation results were found to be in good agreement with the experiments. In the future work, optimization of the device using this numerical model, and a portable driving system based on a 12 V battery and a 12–60 V DC-to-DC converter will be developed.

Acknowledgements This work was supported by the National Science Council (NSC 94-2215-E-006-051) of Taiwan. The authors would like to thank National Center for High-Performance Computing, Tainan, Taiwan, for the support of CFD-ACE+. Additionally, the authors would like to thank the Center for Micro/Nano Science and Technology, and National Nano Device Laboratories, Tainan, Taiwan, for equipment access and technical support. Furthermore, this work made use of Shared Facilities supported by the Program of Top 100 Universities Advancement, Ministry of Education, Taiwan.

References

- C.H. Ahn, M.G. Allen, in *Proceedings of the IEEE Micro Electro Mechanical Systems (MEMS)* 1995, pp. 408–412
- P. Auroux, D. Iossifidis, D. Reyes, A. Manz, *Anal. Chem.* **74**, 2637–2652 (2002)
- S.F. Bart, L.S. Tavrow, M. Mehregany, J.H. Lang, *Sens. Actuators, A*, **21**, 193–197 (1990)
- G. Beni, S. Hackwood, J.L. Jackel, *Appl. Phys. Lett.* **40**(10), 912–914 (1982)
- F. Cattaneo, K. Baldwin, S. Yang, T. Krupenkine, S. Ramachandran, J. A. Rogers, *J. Microelectromech. Syst.* **12**(6), 907–912 (2003)
- S.K. Cho, H. Moon, C.-J. Kim, *J. Microelectromech. Syst.* **12**, 70–80 (2003)
- D. Gueyffier, J. Li, A. Nadim, R. Scardovelli, S. Zaleski, *J. Comput. Phys.* **152**, 423–456 (1999)
- C.W. Hirt, B.D. Nichols, *J. Comput. Phys.* **39**, 201–225 (1981)
- L.-S. Jang, Y.-J. Li, S.-J. Lin, Y.-C. Hsu, W.-S. Yao, M.-C. Tsai, C.-C. Hou, *Biomed. Microdev.* **9**(2), 185–194 (2007)
- C.-J. Kim, *Micropumping by Electrowetting*. (ASME IMECE, New York, 2001) HTD-24200
- C.-S. Liao, G.-B. Lee, J.-J. Wu, C.-C. Chang, T.-M. Hsieh, F.-C. Huang, C.-H. Luo, *Biosens. Bioelectron.* **20**, 1341–1348 (2005)
- J. Lee, C.-J. Kim, *J. Microelectromech. Syst.* **9**(2), 171–180 (2000)
- J. Lee, H. Moon, J. Fowler, T. Schoellhammer, C.-J. Kim, *Sens. Actuators, A* **95**, 259–268 (2002)
- M.G. Lippman, *Ann. Chim. Phys.* **5**, 494–459 (1875)

- W.F. Noh, P.R. Woodward, in *Lecture Notes in Physics*, vol. 59, ed. by A.I. van de Vooren, P.J. Zandbergen (1976), pp. 330–340
- W.J. Rider, D.B. Kothe, *J. Comput. Phys.* **141**, 112–152 (1998)
- W.J. Rider, D.B. Kothe, S.J. Mosso, J.H. Cerrutti, J.I. Hochstein, in *AIAA Paper*, 95-0699 (1995)
- H. Ren, R.B. Fair, M.G. Pollack, *Sens. Actuators, B* **98**, 319–327 (2004)
- D. Reyes, D. Iossifidis, P. Aurox, A. Manz, *Anal. Chem.* **74**, 2623–2636 (2002)
- T. Roques-Carnes, R.A. Hayes, B.J. Feenstra, L.J.M. Schlangen, *J. Appl. Phys.* **95**(8), 4389–4396 (2004)
- T.A. Sammarco, M.A. Burns, *AIChE J.* **45**, 350–366 (1999)
- R. Scardovelli, S. Zaleski, *J. Comput. Phys.* **164**, 228–237 (2000)
- P. Selvaganapathy, Y.-S.L. Ki, P. Renaud, C.H. Mastrangelo, *J. Microelectromech. Syst.* **11**, 448–453 (2002)
- Y.-C. Shu, *Mater. Trans.* **43**(5), 1037–1044 (2002)
- V. Srinivasan, V.K. Pamula, M.G. Pollack, R.B. Fair, in *IEEE 16th Annual International Conference on Micro Electro Mechanical Systems* (2003), pp. 327–330
- J.-H. Tsai, L. Lin, *Sens. Actuator, A*, **97–98**, 665–671 (2002)
- J.P. Van Doormaal, G.D. Raithby, *Numer. Heat Transf.* **7**, 147–163 (1984)
- H.J.J. Verheijen, M.W.J. Prins, *Langmuir* **15**(20) 6616–6620 (1999)
- J. Xie, J. Shih, Q. Lin, B. Yang, Y.C. Tai, *Lab Chip* **4**, 495–501 (2004)
- D.L. Youngs, in *Numerical Methods for Fluid Dynamics*, ed. by K.W. Morton, M.J. Baines (Academic, New York, 1982), pp. 273–285.
- H. Yu, E.S. Kim, in *IEEE International Conference on MEMS, Las Vegas* (IEEE, Los Alamitos, CA, 2002), pp. 125–128
- J. Zeng, T. Korsmeyer, *Lab Chip* **4**, 265–277 (2004)